ACS APPLIED NANO MATERIALS

www.acsanm.org Article

Electrostatic Modulation of Valley Polarization via a Single-Contact Method in Monolayer WSe_2 for Valleytronic Devices

Jyun-Yan Siao, Hong-Li Lin, Tzu-Cheng Lin, Yu-Hsun Chu,* and Minn-Tsong Lin*

Cite This: ACS Appl. Nano Mater. 2025, 8, 7520−7529

Read Online

ACCESS | Metrics & More | Article Recommendations | Supporting Information

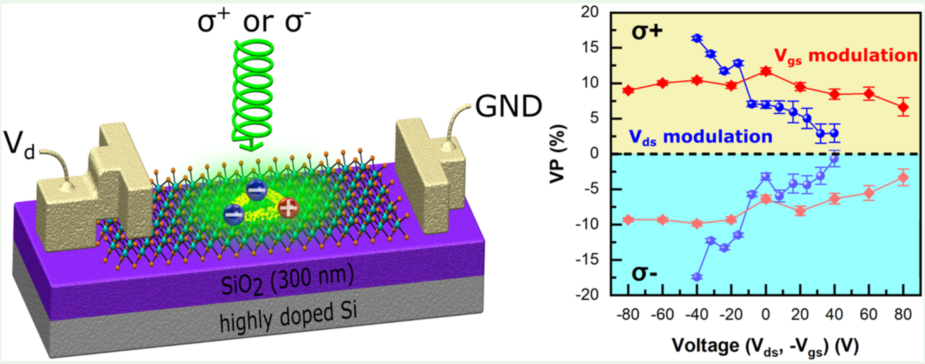

ABSTRACT: The emerging field of valleytronics has sparked significant interest in controlling valley pseudospin in monolayer transition metal dichalcogenides (ML-TMDs). However, maintaining valley polarization (VP) is challenging at high temperatures and during off-resonance excitation. In this study, we introduce an electrostatically tunable single-contact device based on ML-WSe_2, which demonstrates enhanced photoluminescence intensity and VP modulation under off-resonance conditions compared to conventional back-gate methods. Our findings could be illustrated by an electrostatic doping model, which suggests stronger and more uniform doping at the device center. Furthermore, a clear controllability of trion VP switching is also demonstrated over a wide temperature range. The efficient VP control in ML-TMD via the single-contact design enables future applications in valleytronics and optoelectronics.

KEYWORDS: *valleytronics, valley polarization, trion modulation, electrostatic doping, single-contact device, monolayer WSe_2, transition metal dichalcogenides*

■ INTRODUCTION

Valleytronics has garnered significant interest for utilizing valley indices as additional spin-like quantum numbers in momentum space.[1] With inversion symmetry breaking, 1H monolayer transition metal dichalcogenides (ML-TMDs) (0.6−0.75 nm[2,3]), such as MoS_2, $MoSe_2$, WSe_2, and WS_2, feature conduction- and valence-band valleys with opposite valley indices at the K and K' points, leading to valley-dependent optical selection rules.[4−7] The presence of strong spin−orbit coupling (SOC) in ML-TMDs further results in spin splitting and spin-valley locking and allows for spin-selective excitation of specific valleys using circularly polarized light. These properties enable optical control over both the spin and the valley degree of freedom. Furthermore, strong Coulomb interactions in two-dimensional (2D) materials facilitate the formation of excitons and trions.[8] Unlike neutral excitons,[9] trions possess extra charges that enhance exchange interactions, influencing valley relaxation time.[10] This makes them highly stable in preserving valley polarization (VP), which can be quantitatively analyzed via photoluminescence (PL).[4,11−14]

Despite the potential of exciton and trion VP, intervalley scattering, governed by phonon-assisted processes[15−19] and exchange interactions,[20] influences VP and poses challenges for valleytronic devices under ambient conditions. While approaches such as breaking time-reversal symmetry[21−23] and inversion symmetry in bilayer systems[24] have been explored to modify intervalley scattering, these methods typically require large fields or extreme conditions, making them less suitable for continuous switching applications. Recent studies have highlighted electrostatic doping as an alternative for VP control by modulating long-range electron−hole (e-h) screening effects in ML-TMDs.[25−29] Adjusting carrier concentration through electrostatic doping influences Coulomb interactions

Received: December 31, 2024
Revised: March 14, 2025
Accepted: March 27, 2025
Published: April 3, 2025

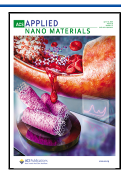

https://doi.org/10.1021/acsanm.4c07356
ACS Appl. Nano Mater. 2025, 8, 7520−7529

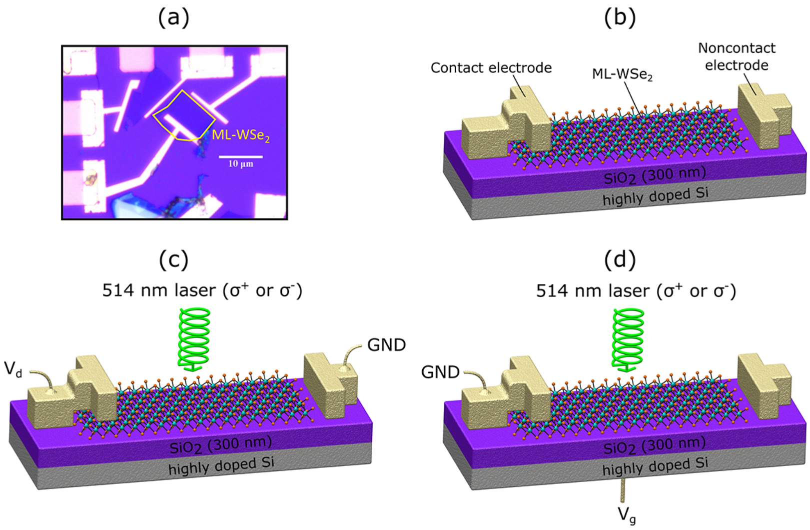

Figure 1. (a) Optical image of a representative exfoliated ML-WSe_2 sample on SiO_2 (300 nm)/Si with a single-contact electrode. (b) Profile of the device showing the single-contact geometry. (c) Circuit diagram illustrating the modulation of drain-source voltage (V_{ds}). (d) Circuit diagram illustrating the modulation of gate voltage (V_{gs}).

governing exciton and trion formation, allowing control over the e-h screening effect, which affect valley relaxation dynamics. However, electrostatic doping via back-gate configurations is limited by Fermi level pinning (FLP) and Schottky barrier height (SBH) at contact, resulting in inefficient charge induction in the channel.[30] These effects arise from interface states at the metal/semiconductor contact, along with potential barriers and an extended depletion zone, which reduce carrier concentration in the channel. Addressing these challenges requires innovative device architectures capable of providing enhanced electrostatic doping effects.

In this work, we present a single-contact device architecture, designed to locally enhance electrostatic doping in ML-WSe_2. This structure demonstrates significantly improved electrostatic doping efficiency, enabling stable and effective VP modulation. Compared to conventional back-gate modulation at 8 K, the single-contact configuration demonstrates better controllability of trion VP, ranging from 3 to 16% within the applied voltage range. We present a model illustrating the electrostatic doping mechanism in the single-contact device, involving efficient charge induction in the central area of ML-TMDs. The VP controllability independent of varied contact conditions is also verified under off-resonance excitation, attributed to higher electrostatic doping efficiency in the V_{ds} circuit. By demonstrating trion VP switching over a broad temperature range under off-resonance excitation, our approach provides a more effective pathway for trion VP modulation, with significant potential for valleytronic and optoelectronic devices using optical and electrical methods to manipulate quantum states in ML-TMD materials.

EXPERIMENTAL SECTION

Sample Preparation and Device Fabrication. Sample of monolayer WSe_2 were mechanically exfoliated from synthetic WSe_2 crystals (2D Semiconductor Ltd.) using PDMS. Samples with a proper lateral size, larger than 8 μm, were chosen and dry-transferred onto heavily doped silicon ($<5 \times 10^{-5}$ $\Omega \cdot$m) covered by a 300 nm layer of SiO_2 substrate. The electrodes were then defined using the standard e-beam lithography technique with PMMA photoresist. To form the electrodes, metals such as Cr (1 nm)/Au (50 nm) or Pt (50 nm) were deposited by thermal evaporation at a deposition rate of 0.5 Å/s under a vacuum $<2 \times 10^{-6}$ mbar. The electrode pattern of the single-contact design includes one electrode directly contacting the WSe_2 sample, which can be either monolayer or multilayer at the contact region, while the measured region remains monolayer. The other electrode is placed directly on the SiO_2 substrate, approximately 1 μm away from the ML-WSe_2.

Measurement. The low-temperature valley polarization measurements were conducted using a home-built system integrated with a circularly polarized excitation and detection module, as well as the high-vacuum 4-probe station (Lake Shore-CRX-EM-HF). For the circularly polarized excitation, a 514 nm laser (photon energy ∼2.41 eV, power of 100 μW) was initially linearly polarized using a polarizer. Subsequently, a quarter-wave plate was employed to generate σ^+ and σ^- polarizations to selectively excite the K or K' valleys. The spot size was focused on the sample to approximately ∼6 μm using a ×10 long working-distance objective (NA = 0.25). The PL measurements primarily reflect the averaged effect over the illuminated area, so the spot sizes do not diminish the validity of our comparisons between different modulation methods.

In the detection process, the emitted photoluminescence from the monolayer WSe_2 sample was analyzed to distinguish between the σ^+ and σ^- components. Initially, the emitted light was collected using the same objective lens, and an achromatic quarter-wave plate converted it into two orthogonally linearly polarized lights. These polarized lights were then analyzed using a linear polarizer. Finally, the σ^+ and σ^- components were detected with a cooled charge-coupled device (CCD). To eliminate the influence of reflected laser light, a long-pass filter was placed in front of the optical fiber connected to the CCD.

For electrical modulation, the Keithley 2636B was utilized to apply either the source-drain voltage (V_{ds}) or the back-gate voltage (V_{gs}). The electrical connection of the device was established using the feedthrough installed on the 4-probe station and then probed with a tungsten tip. For temperature control, the sample could be cooled down to 8 K using a closed-cycle refrigerator with a helium compressor (F-70L) at a pressure level of 1×10^{-6} mbar. Temperature control was achieved through proportional−integral−derivative (PID) control of heaters with an accuracy of 0.01 K.

RESULTS AND DISCUSSION

To enhance the doping effect for VP modulation, we designed a special structure with only one electrode contacting the material, while the other electrode was positioned roughly 1 μm away from ML-WSe_2. This setup is referred to as the single-contact structure in this article. The representative

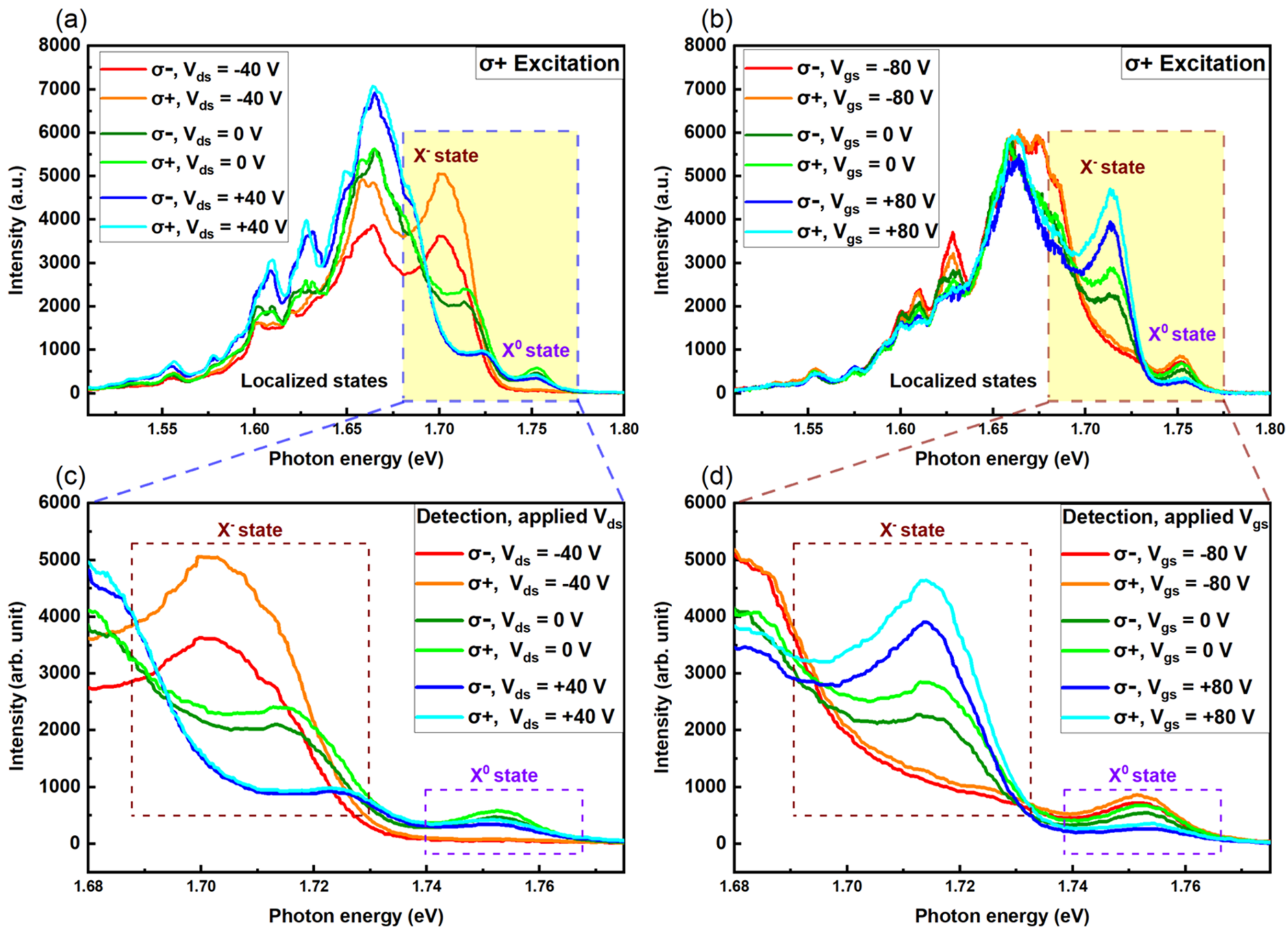

Figure 2. PL response at 8 K with various magnitudes of voltage in V_{ds} and V_{gs} modulation circuits. (a) V_{ds} modulation circuit. (b) V_{gs} modulation circuit. (c),(d) Zoomed-in view of the PL response in the wavelength range of 1.68 to 1.77 eV corresponding to (a),(b), respectively.

device and its profile are shown in Figure 1(a),(b). We utilized a home-built circularly polarized photoluminescence (CPPL) spectroscopy system, combined with a 4-probe station, to study the valley properties of the ML-WSe_2 devices with electrical modulation over a wide temperature range. The devices were initially studied at a temperature of 8 K with a 2.41 eV excitation energy. As illustrated in Figure 1(c),(d), two types of circuits, the V_{ds} circuit and the V_{gs} circuit, were separately used to apply voltage, modulating the doping level of the material in the same device. In the V_{ds} circuit, voltage was applied only between the contact electrode and the noncontact electrode. In contrast, in the V_{gs} circuit, only the contact electrode and the back-gate were connected to the source meter, while the noncontact electrode remained unconnected and did not influence the measurement. Therefore, our measurement approach inherently provides a direct comparison between configurations with and without the noncontact electrode within the same device, ensuring an identical 300 nm SiO_2 dielectric and enabling an independent evaluation while minimizing variations due to fabrication differences.

In Figure 2, the ML-WSe_2 is excited by right-hand circularly polarized (σ^+) light, and both σ^+ and σ^- detections are performed to measure the emission from the K and K' valleys. At a temperature of 8 K, two well-defined optical states were identified in our experiments. One is the neutral exciton (X^o), observed at around 1.753 eV, and the other is the trion (X^-), observed at around 1.715 eV with zero voltage. These states are highlighted in the yellow areas in Figure 2(a),(b), with zoom-in views in (c)-(d), respectively. Due to its 2D nature, the strong Coulomb interaction tightly binds the excited electrons and holes together, forming an exciton state with a very large binding energy of a few hundred meV.[31−33] Additionally, the trion is a three-particle system formed by an exciton with an extra negative or positive carrier in the material,[8,34] emitting lower PL energy. Typically, the binding energy of a trion can be directly determined from the energy difference between the neutral exciton and the trion, which was calculated to be 38 meV in our case. This value is in agreement with the literature, which reports a range of 30−40 meV.[27]

The zoomed-in spectra ranging from 1.68 to 1.77 eV in Figure 2(c),(d) exhibit a PL intensity difference between the σ^+ and σ^- detections at the exciton and trion states, providing evidence of valley polarization. Moreover, with different magnitudes of V_{ds} or V_{gs}, the PL intensity difference between σ^- and σ^+ detections varies for the X^o and X^- states, indicating that the value of valley polarization is modulated by both V_{ds} and V_{gs} circuits. Additionally, the increasing (decreasing) trend of PL intensities is opposite with the V_{ds} and V_{gs} modulation, which is due to the opposite carrier charging type, and will be discussed in detail later. Apart from this, spectral features lower than 1.69 eV likely originate from localized states.[9,35,36] Not

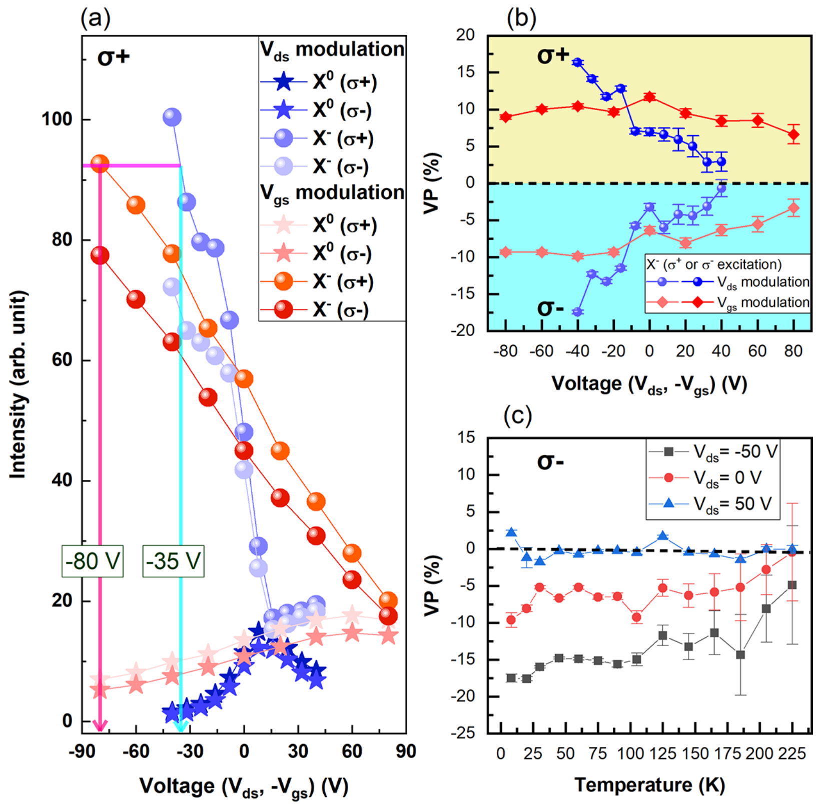

Figure 3. (a) Intensities extraction of X^o and X^- states under V_{ds} and V_{gs} modulation at 8 K. Higher voltage is necessary in V_{gs} (∼80 V) to reach the same level of intensity as in V_{ds} (∼35 V) circuit. (b) Voltage-dependent VP measurements with V_{ds} and V_{gs} modulation at 8 K. Shadow colors of caramel and bright blue correspond to different circularly polarized light excitations, demonstrating time-reversal symmetry in the ML-WSe_2 system. (c) Temperature-dependent VP measurements with V_{ds} modulation at selected voltages.

consistently found in different devices and not stable and well-controlled by electrical modulation, these features are not discussed in this article. However, to mitigate concerns about potential contributions from localized states, we provide CPPL spectra at 60 K (Supporting Information, Figure S1), where localized state emission is reduced due to thermal activation. This suggests that the observed effect primarily arises from electrical modulation rather than localized state involvement. More details of V_{ds} and V_{gs} voltage sweeping were also conducted at 8 K, and the corresponding X^o and X^- peak intensities are extracted and plotted in Figure 3(a). Note that, for comparison, the polarity of V_{gs} is directly reversed to have the same charging carrier type as V_{ds} modulation. In addition to the voltage-modulated X^o and X^- PL intensities in both σ^+ and σ^- detections, a smaller voltage is required for the same level of PL enhancement in V_{ds} compared to V_{gs} modulations, as marked by the red and blue guide lines in Figure 3(a). This suggests that electrical modulation has a stronger influence in the V_{ds} case than in the V_{gs} case.

To quantify the circularity of PL emission, the degree of valley polarization is calculated with an equation[37]

$$\mathrm{VP} = \frac{I(\sigma^+) - I(\sigma^-)}{I(\sigma^+) + I(\sigma^-)} \times 100\% \quad (1)$$

where $I(\sigma^+)$ and $I(\sigma^-)$ denote the PL peak intensities of right and left circularly polarized components, respectively. In this article, we focus on the modulation effect on the trion state, as it is more directly affected by electrostatic doping due to its charging property. Although we can observe the valley polarization of the exciton (∼10%), the electrically induced change in PL intensity is at the same level as the noise, causing large uncertainties in the VP calculation. To illustrate the impact of electrostatic doping on trion valley polarization, Figure 3(b) shows the comparison of V_{ds} and V_{gs} modulation on the trion VP. Notably, in the V_{ds} modulation case (blue data points), a higher VP of P ∼ 16% is achieved as WSe_2 is subjected to negative voltage, while a lower VP (∼3%) is tuned with positive voltage. In contrast, in the V_{gs} modulation case (red data points), although it shows slightly higher/lower values under negative/positive voltage, the trend is not obvious in controlling VP. Consequently, electrical modulation is more apparent in V_{ds} tuning with a single-contact configuration, enabling control over both PL intensity and valley polarization. Our results demonstrate a clear on/off operation in the devices (Supporting Information, S2), yielding average VP of (16.4 ± 3.4)% in the ON state and of (2.2 ± 1.9)% in the OFF state. This consistency is crucial for the development of valleytronic and optoelectronic devices. Additionally, the CPPL measurements performed with both σ^+ and σ^- excitations confirm the time-reversal symmetry of the valley, as observed in Figure 3(b).

To further verify the trion VP on/off operation and controllability using V_{ds} circuits, Figure 3(c) presents detailed temperature-dependent VP measurements at selected voltages. Across a wider temperature range, up to 225 K, the trion VP is well modulated and clearly distinguished by the polarity of V_{ds}, suggesting that phonon-induced intervalley scattering is effectively modified,[16,38,39] thereby demonstrating effective manipulation of the valley degree of freedom. However, the VP values still decrease with increasing temperature as higher

https://doi.org/10.1021/acsanm.4c07356
ACS Appl. Nano Mater. 2025, 8, 7520−7529

thermal energy dissociates trion states by overcoming their binding energy, resulting in a decrease in trion PL intensity. Additionally, stronger phonon-assisted scattering becomes more prominent as the temperature increases, directly causing a reduction in VP. These factors together lead to larger error bars in the VP calculation at higher temperatures.

As demonstrated, the single-contact configuration can exhibit intensity and VP-modulated effects, even surpassing the conventional back-gate method. Our results suggest that the noncontact electrode modifies the local electric field distribution in the measured region, leading to more localized and efficient electrostatic doping. To further explain the electrical tuning effect in the single-contact configuration, we propose a model, as shown in Figure 4. First, we consider an effective circuit consisting of two metal−insulator−metal (MIM) structures and one metal−insulator-semiconductor (MIS) structure. One of the former capacitors, named the contact capacitor (C_C), originates from the contact side metal and the highly doped silicon underneath, acting as a metallic layer. The other capacitor, named the noncontact capacitor (C_N), results from the noncontact side metal and the highly doped silicon underneath. The charge distribution in the highly doped silicon is thus attributed to electrostatic induction, and C_C and C_N can stabilize and make the charge distribution underneath the middle region of ML-WSe_2 more uniform. In the middle area of the device, marked by a red dashed line in Figure 4(a), an MIS structure is formed by ML-WSe_2 and highly doped silicon, with 300 nm silicon oxide in between. We assume that the middle ML-WSe_2 region has a potential comparable to the contact side electrode due to the influence of the C_N capacitor. This creates a potential difference between the TMDs and the highly doped silicon, leading to a more localized and enhanced electrostatic doping effect in the middle region. Compared to the conventional back-gate circuit, which is a more global gating method and may be limited by the FLP effect, making electrostatic doping less efficient, the single-contact circuit provides a stronger local depletion region in the middle of the ML-WSe_2. Additionally, we neglect the capacitance between the right edge of ML-WSe_2 and the noncontact electrode (vacuum gap, $\epsilon_{vacuum} \sim 1$, $d_{vacuum} \sim 1\ \mu m$), as a simple parallel plate capacitor approximation suggests that the induced carrier concentration would be approximately an order of magnitude smaller ($\sim$1000/300 × 3.9) than that of the SiO_2 layer ($\epsilon_{SiO_2} \sim 3.9$, $d_{SiO_2} \sim 300$ nm). Since most of the voltage drop occurs across the vacuum gap, the resulting lateral electric field within the material, which could lead to lateral depletion and nonuniform charge distribution, should also be negligible.

To illustrate the charge distribution under electrostatic doping using a single-contact circuit, consider a negative V_{ds} voltage as an example. When negative voltage is applied between the contact and noncontact electrodes, the equilibrium charge distribution, as shown in Figure 4(a), results in negative charge doping in the measured region. Figure 4(b) presents a schematic band diagram of the MIS region, where excitation and emission processes occur, consisting of ML-WSe_2/SiO_2/heavily doped silicon under thermal equilibrium conditions. In this diagram, ϕ_m represents the work function of heavily doped silicon,[40] χ_i denotes the electron affinity of SiO_2,[41] and χ_s corresponds to the electron affinity of monolayer WSe_2.[42] Similar diagrams have been employed in previous studies to conceptualize potential modulation in 2D materials under gating configurations.[43−46] To describe the electrostatic doping effect, in the following discussion, V_{ds} is considered positive ($V > 0$) when a monolayer WSe_2 is positively biased with respect to the noncontact electrode. For simplicity, we assume that interfacial trap states at the ML-WSe_2/SiO_2 interface do not play a dominant role and that no carrier transport occurs in any region between the defined electrodes when V_{ds} is applied. While charge trapping may still exist,[47] both configurations experience the same interface conditions. The stronger VP modulation in the V_{ds} circuit suggests that electrostatic doping is the dominant mechanism, so interfacial states are not considered in our schematic. Moreover, since electrostatic modulation primarily occurs through the MIS structure, with negligible capacitance formed

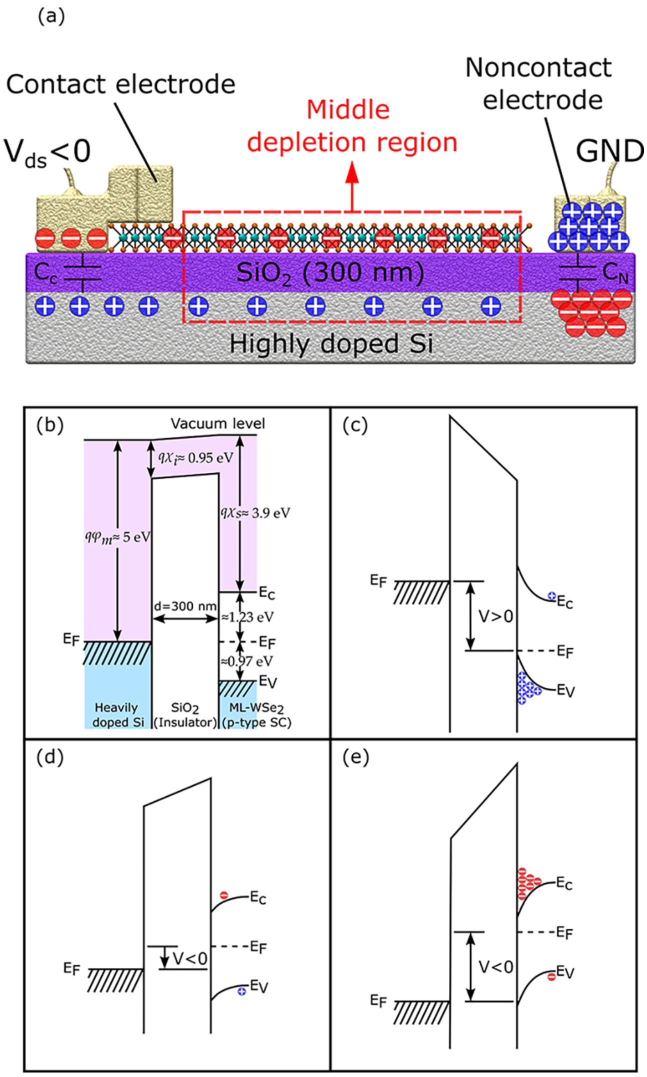

Figure 4. (a) Illustration of charge distribution under the $V_{ds} < 0$ condition. C_C and C_N refer to the coupled capacitors at the contact and noncontact sides, respectively. Schematic band diagram near the interface of ML-WSe_2/SiO_2/heavily doped silicon. (b) At thermal equilibrium, where ϕ_m is the work function of heavily doped Si;[40] χ_i is the electron affinity of SiO_2;[41] χ_s is the electron affinity of a monolayer WSe_2,[42] and d is the thickness of the SiO_2 dielectric layer. (c) Accumulation case: when $V_{ds} > 0$ is applied, hole carriers accumulate at the semiconductor surface. (d) Depletion case: with a proper small $V_{ds} < 0$ applied, hole carriers decrease while electron carriers increase. (e) Inversion case: when a larger $V_{ds} < 0$ is applied, the electron carriers increase rapidly.

https://doi.org/10.1021/acsanm.4c07356
ACS Appl. Nano Mater. 2025, 8, 7520−7529

by vacuum, the band diagrams for V_{ds} and V_{gs} would appear similar due to the dominance of the vertical electric field. However, the V_{ds} circuit induces stronger band bending with smaller V_{ds} voltages, as supported by carrier concentration estimates (Supporting Information, Figure S3), leading to significantly enhanced electrostatic doping efficiency. Thus, three possible band diagrams of the MIS region, with different V_{ds} voltages applied, are illustrated in Figure 4(c)−(e), depicting the redistribution of carriers and the electrostatic doping mechanisms enabled by the single-contact configuration.

In Figure 4(c), when a positive V_{ds} is applied ($V_{ds} > 0$) to a monolayer WSe_2, the valence-band edge, E_v, will bend upward near the monolayer WSe_2 surface, approaching the Fermi level. Importantly, since the carrier density is exponentially related to the energy difference ($E_F - E_v$) according to the Fermi−Dirac distribution, we can expect that the majority carrier (holes) will accumulate near the monolayer WSe_2 surface due to band bending. This is known as the accumulation case when a monolayer WSe_2 is positively biased. Figure 4(d) illustrates the depletion case when a small negative bias ($V_{ds} < 0$) is applied. The band near the monolayer WSe_2 gradually bends downward, inducing more minority carriers (electrons). When the negative bias increases further, the band inclines even more downward, as shown in Figure 4(e). In other words, the polarity of the charge carriers changes from majority (holes) to minority (electrons), representing the inversion case, which corresponds to the charge distribution shown in Figure 4(a). As discussed above, when $V_{ds} < 0$ ($V_{ds} > 0$), the electron (hole) carriers are induced, respectively. This contrasts with the conventional definition in back-gate devices, where, for $V_{gs} > 0$ ($V_{gs} < 0$), the electron (hole) carriers get charged in the material. Therefore, the polarity of V_{gs} in Figure 3(a),(b) is reversed for comparisons under the same charging type. As a result, we attribute the V_{ds} electrostatic doping effect to enhanced band bending in the middle of ML-WSe_2, facilitated by the coupling of the C_C and C_N capacitors.

In Figure 3(b), it is shown that the trion VP exhibits a pronounced switching effect using the V_{ds} circuit. This is likely due to the depletion region in the middle, which contributes to more effective electrostatic doping locally and results in a significant on/off operation. This contrasts with the V_{gs} circuit case, where the depletion region is weaker in the middle due to global gating and is further limited by contact conditions. In general, the modulation of valley polarization using electrostatic doping can result from the suppression of intervalley scattering, which is related to the screening effect of long-range e-h interactions. This mechanism originates from the Maialle−Silva−Sham mechanism, describing the depolarization process of exciton spin in semiconductors.[48,49] It has also been shown that electron−hole interactions dominate as the primary relaxation mechanism of the valley pseudospin of bright excitons.[29] Theoretically, the valley polarization of excitons and trions can be derived from a rate equation, and under the steady state, the equation is given by[16,17,37]

$$\mathrm{VP}_{X^o} = \frac{\mathrm{VP}_0}{1 + \frac{\tau_{X^o}}{\tau_{V_{X^o}}}} \times 100\% \tag{2}$$

$$\mathrm{VP}_{X^-} = \frac{\mathrm{VP}_{X^o}}{1 + \frac{\tau_{X^-}}{\tau_{V_{X^-}}}} \times 100\% \tag{3}$$

where VP_0 is the initial polarization of the exciton, VP_{X^o} and VP_{X^-} are the valley polarization of the exciton and trion, respectively; τ_{X^o} and τ_{X^-} denote the recombination time of the exciton and trion; and $\tau_{V_{X^o}}$ and $\tau_{V_{X^-}}$ represent the intervalley relaxation time of the exciton and trion. Therefore, the valley polarization of the trion VP_{X^-} is determined by several factors such as VP_0, the ratio of $\tau_{X^o}/\tau_{V_{X^o}}$, and the ratio of $\tau_{X^-}/\tau_{V_{X^-}}$. Additionally, VP_0 is mainly affected by excitation energy.[17] When discussing the origin of trion valley polarization, one can consider VP_0 as a fixed value. Consequently, the valley polarization of the trion is influenced by the exciton and trion recombination time, along with their valley relaxation mechanism, which determines the ratios of $\tau_{X^o}/\tau_{V_{X^o}}$ as well as $\tau_{X^-}/\tau_{V_{X^-}}$. The exciton valley relaxation time τ_v is correlated with the Thomas-Fermi wave vector $k_{TF}(T,E_F) = k_{TF0}[1 - \exp(-E_F/k_BT)]$ for 2D electron gas.[28] $k_{TF0} = g_s g_v m_e c^2/(4\pi\varepsilon\hbar^2)$ denotes a zero-temperature Thomas wave vector, in which g_s and g_v are the degeneracy for spin and valley indexes, respectively, m^* is the effective mass of electron or hole, ε is the dielectric constant, $\hbar = h/2\pi$ is Planck's constant, k_B is Boltzmann's constant, and T is temperature. E_F is related to the doped electron (hole) density, $n_c = g_s g_v m_e E_F/(2\pi\hbar^2)$. Importantly, the inverse of k_{TF} can be used to describe the screening length due to long-range e-h interaction in the electrostatic doping system, which is expressed by, $\frac{1}{\tau_v} = \frac{AJ^2\Gamma_h}{\hbar}\frac{1}{k_{TF}^2}$,[28,29] where $A = 9a^2M^2/4\pi^2\hbar^4$ is a material-dependent parameter, in which a is the lattice constant, and M is the exciton mass, Γ_h is the homogeneous line width of excitons, and J is the strength of the exchange interaction. Under this theoretical framework, when the carrier density is increased by electrostatic doping, the Fermi energy is elevated, resulting in an increase of k_{TF}. This indicates the screening length will decrease as carrier density increases, suppressing the intervalley scattering, and thus the valley relaxation time increases. Consequently, the valley polarization can be enhanced or reduced by the modulation of valley relaxation time using electrostatic doping. In the previous report,[25] Shinokita et al. has shown that the exciton recombination time is V_{gs}-independent, but longer valley relaxation time is observed as doped by V_{gs} modulation, leading to higher valley polarization.

Although long-range e-h interactions can directly influence the exciton dynamics, their impact on trions is relatively indirect, making it challenging to predict trion dynamics within this theoretical framework. However, this framework suggests that understanding the competition between τ_{X^o}, $\tau_{V_{X^o}}$, τ_{X^-}, and $\tau_{V_{X^-}}$ is crucial for describing the trion VP. In our opinion, the trion VP is primarily influenced by the ratio of $\tau_{X^-}/\tau_{V_{X^-}}$ as the carrier density rapidly decreases. This effect arises from a decrease in $\tau_{V_{X^-}}$, likely due to more available states potentially being filled in the opposite valley, a consequence of the reduced screening effect. Therefore, an increase in the ratio $\tau_{X^-}/\tau_{V_{X^-}}$ leads to a reduction in the trion VP. In contrast, as the carrier density increases, the ratio $\tau_{X^-}/\tau_{V_{X^-}}$ could approach zero, causing VP to be predominantly governed by VP_{X^o}. This suggests that the reduction/enhancement of $\tau_{V_{X^-}}$, caused by lower/higher carrier density, plays a significant role in the off/on state of the trion VP.

https://doi.org/10.1021/acsanm.4c07356
ACS Appl. Nano Mater. 2025, 8, 7520−7529

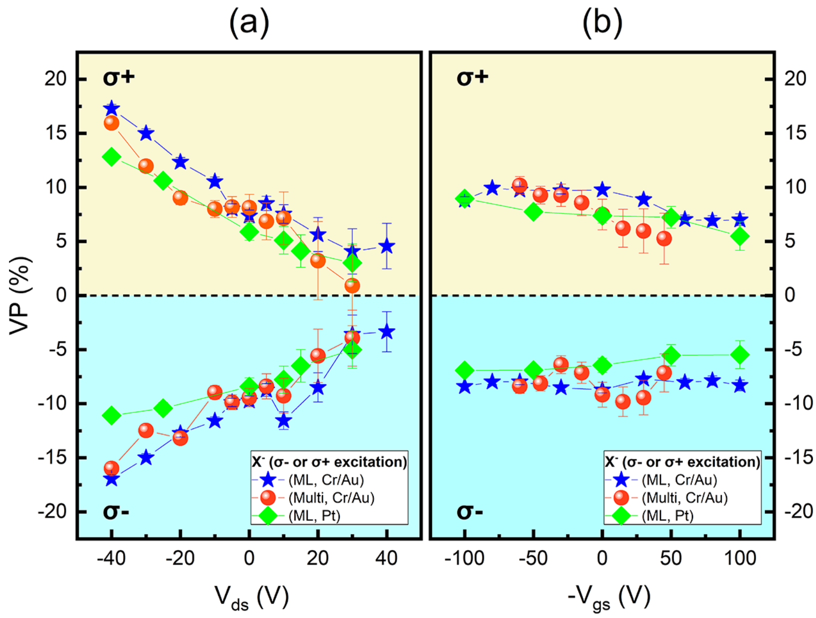

Figure 5. Voltage-dependent VP measurements in (a) V_{ds}- and (b) V_{gs}-modulated circuits with different contact conditions.

Furthermore, compared to the 2D back-gate device, the V_{ds} electrical modulation effect focuses on the electrostatic doping in the middle area of ML-TMDs, which provides a more uniform and larger effective modulation region. In contrast, in a 2D back-gate device, not only is the electrostatic doping globally weaker, but one must also consider the properties of the contact side, such as the presence of numerous interfacial states or metal-induced gap states at the metal/TMD interface, which cause the FLP effect.[50−52] These factors limit the V_{gs} modulation efficiency in the middle area of the sample, resulting in less effective electrical modulation. On the other hand, when V_{ds} is applied in a single-contact configuration, a similar situation can occur in the contact region, as in the V_{gs} modulation case. While this may reduce the efficiency of electrical modulation, the noncontact electrode enables a more localized and stronger electric field in the MIS region, enhancing electrostatic doping in ML-WSe_2 and facilitating effective VP modulation, as shown in Figure 3(c).

To further discuss the difference between V_{ds} and V_{gs} modulation efficiencies, we estimated the carrier concentration at higher temperatures using the mass action law,[25,53−57] as shown in Figure S3 (Supporting Information). The results reveal that the V_{ds} circuit achieves carrier concentrations nearly an order of magnitude higher than the V_{gs} circuit, even with lower V_{ds} voltages. This aligns with our observations of enhanced PL intensity and VP modulation in the V_{ds} configuration. Therefore, while both V_{ds} and V_{gs} circuits may be affected by the FLP effect near the contact area, the V_{ds} circuit provides a stronger modulation area in the middle, enhancing overall efficiency. Consequently, the modulation effects on PL and VP using the V_{ds} circuit primarily originate from the stronger electrostatic doping effect in the middle of ML-WSe_2, suggesting a negligible contribution from contact properties.

To validate our speculation, we altered the contact conditions by fabricating three types of devices: (1) Cr/Au contact on ML-WSe_2, (2) Cr/Au contact on the multilayer region of WSe_2,[58−60] and (3) Pt contact on ML-WSe_2,[61,62] while ensuring that the measured region remained monolayer in all cases. This aimed to change the work function to a lower SBH and partially mitigate FLP effect. However, Figure 5(a) demonstrates that the trends in VP modulation are not significantly different across the series with the V_{ds} circuit, and all of them show a clear on/off switching effect. Therefore, despite differences in contact conditions across devices, valley polarization modulation follows the same trend, suggesting that, in the V_{ds} circuit, the observed effect is primarily driven by stronger electrostatic doping in the middle of ML-WSe_2 rather than by specific contact properties. The results agree with our speculation that the contact conditions do not dominate the electrostatic doping effect. While the single-contact circuit does not fully solve inherent contact issues, the incorporation of C_C and C_N coupling may generate a more localized and stronger electric field, leading to charge redistribution and enhanced electrostatic doping in regions away from the contact side. Additionally, under the same excitation condition (detuning energy ∼ 700 meV), Figure 5(b) shows no clear modulation trend across the series due to lower electrostatic doping using the V_{gs} circuit, where lower doping levels are less effective due to increased phonon activity enhancing intervalley scattering,[17] even with changes in the contact conditions. Thus, the single-contact circuit not only facilitates a more feasible device design but also alleviates concerns of contact fabrication issues while concurrently maintaining a high level of efficiency in electrical modulation.

It is noted that using a thinner dielectric layer can also lead to improvements with the V_{gs} circuit. However, the contact issues originating from FLP and SBH still remain, limiting the metal material selection and charging efficiency. Additionally, using a thinner oxide substrate increases the risk of device breakdown due to the higher electric field around the contact region. In our study, we adopted a 300 nm SiO_2 dielectric layer with the V_{ds} circuit, which not only enhances the PL and VP modulation but also reduces the risk of device breakdown, further indicating the advantage of the single-contact configuration. Moreover, in reality, there might be some interfacial states at the TMD and SiO_2 interface,[43,47] which may significantly affect the modulation efficiency. Our results

https://doi.org/10.1021/acsanm.4c07356
ACS Appl. Nano Mater. 2025, 8, 7520−7529

demonstrate explicit on/off switching operation, suggesting that higher electrostatic doping with a single-contact circuit may mitigate this issue. This enhancement arises as a higher doping level initially saturates most interfacial states, reducing their impact, and subsequently adjusts the Fermi level in the MIS region, thereby enhancing PL and VP modulation efficiency.

While our study employs a SiO_2 dielectric for back-gate control, previous studies[63−65] have shown that using hBN as a gate dielectric can enhance electrostatic doping efficiency due to its cleaner interface with 2D materials and reduced charge trapping.[66,67] This improved interface quality enables more effective electrostatic control and allows for the use of a thinner hBN gate layer, leading to higher carrier concentration under a lower applied voltage and facilitating the investigation of excitonic and valleytronic phenomena.[26] Moreover, the single-contact method is compatible with previous device architectures such as hBN/Graphene heterostructure,[68] potentially further enhancing doping efficiency.

Beyond dielectric effects, VP values reported in previous studies also vary due to differences in materials,[25] excitonic states,[68] and detuning energies,[17] making direct comparisons of absolute values less meaningful. For instance, our study was conducted at a larger detuning energy (∼700 meV), where phonon-assisted intervalley scattering suppresses initial VP, inherently leading to lower absolute VP values.[17] Instead of comparing absolute VP, we evaluate the modulation efficiency through the on/off ratio. In Figure 3(b), we find that the V_{ds} circuit achieves a better on/off ratio of 16.3/2.9 ∼ 5.6 at 8 K, compared to 6.1/3.3 ∼ 1.8 in the V_{gs} case. Furthermore, Figure 3(c) suggests that the on/off ratio could be further enhanced at higher applied voltages, where the off-state approaches zero, indicating the potential for an even greater VP contrast. These results highlight the effectiveness of the single-contact approach in electrostatic doping control.

Overall, our results clearly demonstrate that, even though the excitation energy (∼2.41 eV) is far from the optical band gap energy (trion ∼1.71 eV at 8 K), where ∼700 meV detuning energy is present, the modulation effect is still significant. Importantly, distinguishable states of valley polarization can still be observed up to 225 K, marking progress in controllable valley polarization using a single-contact configuration under off-resonance excitation. This approach requires only ML-WSe_2 on a standard SiO_2 dielectric, which already exhibits a stronger electrostatic doping effect, facilitating integration into large-scale 2D heterostructures. Additionally, it is adaptable to existing device architectures, making it valuable for exploring phenomena at higher doping levels. Beyond demonstrating effective electrostatic doping and valley polarization modulation, this work establishes the single-contact method as a promising approach for TMD-based valleytronic and optoelectronic applications, offering a practical and scalable strategy for device development.

■ CONCLUSIONS

In summary, we have developed a single-contact device to effectively manipulate the valley degree of freedom in monolayer WSe_2 using electrostatic doping. Our proposed model, based on an MIS-like mechanism, illustrates how this configuration achieves more uniform charge distribution in the middle of the device, leading to better control of both PL intensity and VP. Compared to the conventional back-gate circuit, the single-contact device demonstrates notable performance, achieving clear on/off switching of trion VP (ranging from ∼3 to 16% at 8 K) under off-resonance excitation (∼2.41 eV) with a large detuning energy (∼700 meV). This effective switching remains stable across a wide temperature range (8 to 225 K), attributed to the modulation of the long-range e-h screening effect, which reduces phonon-induced intervalley scattering. Moreover, our findings using single-contact method suggest that contact conditions have minimal impact on PL and VP modulation, thereby reducing concerns related to SBH and FLP, presenting an alternative method for effective electrical modulation. These results validate the stability and efficiency of the single-contact device in manipulating valley polarization through electrostatic doping and demonstrate its capability for enhanced VP modulation and trion switching across a broad temperature range. This establishes the single-contact method as a promising strategy for valleytronic applications, enabling effective VP modulation in ML-TMD materials and opening new avenues for advanced valleytronic and optoelectronic device design.

■ ASSOCIATED CONTENT

Supporting Information

The Supporting Information is available free of charge at https://pubs.acs.org/doi/10.1021/acsanm.4c07356.

PL spectra at 60 K with selected V_{ds} voltages for valley polarization modulation; reproducible on/off switching behavior of valley polarization across three devices; detailed calculation of utilizing the mass action law to evaluate carrier concentration (PDF)

■ AUTHOR INFORMATION

Corresponding Authors

Yu-Hsun Chu − *Department of Physics, National Taiwan University, Taipei 10617, Taiwan;* orcid.org/0000-0002-2893-2016; Email: yuhsunchu@gmail.com

Minn-Tsong Lin − *Department of Physics, National Taiwan University, Taipei 10617, Taiwan; Institute of Atomic and Molecular Sciences, Academia Sinica, Taipei 10617, Taiwan; Research Center for Applied Sciences, Academia Sinica, Taipei 11529, Taiwan;* orcid.org/0000-0001-7735-4219; Email: mtlin@phys.ntu.edu.tw

Authors

Jyun-Yan Siao − *Department of Physics, National Taiwan University, Taipei 10617, Taiwan;* orcid.org/0009-0003-5072-9019

Hong-Li Lin − *Department of Physics, National Taiwan University, Taipei 10617, Taiwan*

Tzu-Cheng Lin − *Department of Physics, National Taiwan University, Taipei 10617, Taiwan*

Complete contact information is available at: https://pubs.acs.org/10.1021/acsanm.4c07356

Author Contributions

J.-Y.S. and M.-T.L. designed and prepared the experiment. J.-Y.S., H.-L.L., and T.-C.L. carried out device fabrication, CPPL setup/measurements, electrical measurements, and data analysis. J.-Y.S. coded CPPL and electrical measurement programs. Y.-H.C. and M.-T.L. supervised the study. The manuscript was drafted by J.-Y.S., and revised and edited by Y.-

H.C. and M.-T.L. The project was conceived and led by M.-T.L.

Notes

The authors declare no competing financial interest.

■ ACKNOWLEDGMENTS

This work was supported by the National Science and Technology Council (NSTC), Taiwan, under grant number NSTC 112-2112-M-002-046-MY3. The authors thank Dr. Yu-Ming Chang, Dr. Wei-Liang Chen, Yu-Chun Huang, and the staff at the Photonic Workshop, Center for Condensed Matter Sciences, National Taiwan University, Taipei 10617, Taiwan, for their technical assistance.

■ REFERENCES

(1) Schaibley, J. R.; Yu, H.; Clark, G.; Rivera, P.; Ross, J. S.; Seyler, K. L.; Yao, W.; Xu, X. Valleytronics in 2D materials. *Nat. Rev. Mater.* **2016**, *1*, No. 16055.

(2) Qi, J.; Lan, Y.-W.; Stieg, A. Z.; Chen, J.-H.; Zhong, Y.-L.; Li, L.-J.; Chen, C.-D.; Zhang, Y.; Wang, K. L. Piezoelectric effect in chemical vapour deposition-grown atomic-monolayer triangular molybdenum disulfide piezotronics. *Nat. Commun.* **2015**, *6*, No. 7430.

(3) Okada, M.; Okada, N.; Chang, W.-H.; Endo, T.; Ando, A.; Shimizu, T.; Kubo, T.; Miyata, Y.; Irisawa, T. Gas-Source CVD Growth of Atomic Layered WS_2 from WF_2 and H_2S Precursors with High Grain Size Uniformity. *Sci. Rep.* **2019**, *9*, No. 17678.

(4) Xiao, D.; Liu, G.-B.; Feng, W.; Xu, X.; Yao, W. Coupled Spin and Valley Physics in Monolayers of MoS_2 and Other Group-VI Dichalcogenides. *Phys. Rev. Lett.* **2012**, *108*, No. 196802.

(5) Zhu, Z. Y.; Cheng, Y. C.; Schwingenschlögl, U. Giant spin-orbit-induced spin splitting in two-dimensional transition-metal dichalcogenide semiconductors. *Phys. Rev. B* **2011**, *84*, No. 153402.

(6) Cheiwchanchamnangij, T.; Lambrecht, W. R. L. Quasiparticle band structure calculation of monolayer, bilayer, and bulk MoS_2. *Phys. Rev. B* **2012**, *85*, No. 205302.

(7) Yao, W.; Xiao, D.; Niu, Q. Valley-dependent optoelectronics from inversion symmetry breaking. *Phys. Rev. B* **2008**, *77*, No. 235406.

(8) Mak, K. F.; He, K.; Lee, C.; Lee, G. H.; Hone, J.; Heinz, T. F.; Shan, J. Tightly bound trions in monolayer MoS_2. *Nat. Mater.* **2013**, *12*, 207−211.

(9) Zhu, C. R.; Zhang, K.; Glazov, M.; Urbaszek, B.; Amand, T.; Ji, Z. W.; Liu, B. L.; Marie, X. Exciton valley dynamics probed by Kerr rotation in WSe_2 monolayers. *Phys. Rev. B* **2014**, *90*, No. 161302.

(10) Yan, T.; Yang, S.; Li, D.; Cui, X. Long valley relaxation time of free carriers in monolayer WSe_2. *Phys. Rev. B* **2017**, *95*, No. 241406.

(11) Splendiani, A.; Sun, L.; Zhang, Y.; Li, T.; Kim, J.; Chim, C.-Y.; Galli, G.; Wang, F. Emerging Photoluminescence in Monolayer MoS_2. *Nano Lett.* **2010**, *10*, 1271−1275.

(12) Mak, K. F.; Lee, C.; Hone, J.; Shan, J.; Heinz, T. F. Atomically Thin MoS_2: A New Direct-Gap Semiconductor. *Phys. Rev. Lett.* **2010**, *105*, No. 136805.

(13) Gutiérrez, H. R.; Perea-López, N.; Elías, A. L.; Berkdemir, A.; Wang, B.; Lv, R.; López-Urías, F.; Crespi, V. H.; Terrones, H.; Terrones, M. Extraordinary Room-Temperature Photoluminescence in Triangular WS_2 Monolayers. *Nano Lett.* **2013**, *13*, 3447−3454.

(14) Zhao, W.; Ghorannevis, Z.; Chu, L.; Toh, M.; Kloc, C.; Tan, P.-H.; Eda, G. Evolution of Electronic Structure in Atomically Thin Sheets of WS_2 and WSe_2. *ACS Nano* **2013**, *7*, 791−797.

(15) Mai, C.; Semenov, Y. G.; Barrette, A.; Yu, Y.; Jin, Z.; Cao, L.; Kim, K. W.; Gundogdu, K. Exciton valley relaxation in a single layer of WS_2 measured by ultrafast spectroscopy. *Phys. Rev. B* **2014**, *90*, No. 041414.

(16) Hanbicki, A.; Kioseoglou, G.; Currie, M.; Hellberg, C. S.; McCreary, K.; Friedman, A.; Jonker, B. Anomalous temperature-dependent spin-valley polarization in monolayer WS_2. *Sci. Rep.* **2016**, *6*, No. 18885.

(17) Kioseoglou, G.; Hanbicki, A. T.; Currie, M.; Friedman, A. L.; Gunlycke, D.; Jonker, B. T. Valley polarization and intervalley scattering in monolayer MoS_2. *Appl. Phys. Lett.* **2012**, *101*, No. 221907.

(18) Prazdnichnykh, A. I.; Glazov, M. M.; Ren, L.; Robert, C.; Urbaszek, B.; Marie, X. Control of the exciton valley dynamics in atomically thin semiconductors by tailoring the environment. *Phys. Rev. B* **2021**, *103*, No. 085302.

(19) Stier, A. V.; Wilson, N. P.; Clark, G.; Xu, X.; Crooker, S. A. Probing the Influence of Dielectric Environment on Excitons in Monolayer WSe_2: Insight from High Magnetic Fields. *Nano Lett.* **2016**, *16*, 7054−7060.

(20) Yu, H.; Liu, G.-B.; Gong, P.; Xu, X.; Yao, W. Dirac cones and Dirac saddle points of bright excitons in monolayer transition metal dichalcogenides. *Nat. Commun.* **2014**, *5*, No. 3876.

(21) Srivastava, A.; Sidler, M.; Allain, A. V.; Lembke, D. S.; Kis, A.; Imamoğlu, A. Valley Zeeman effect in elementary optical excitations of monolayer WSe_2. *Nat. Phys.* **2015**, *11*, 141−147.

(22) Norden, T.; Zhao, C.; Zhang, P.; Sabirianov, R.; Petrou, A.; Zeng, H. Giant valley splitting in monolayer WS_2 by magnetic proximity effect. *Nat. Commun.* **2019**, *10*, No. 4163.

(23) Zhong, D.; Seyler, K. L.; Linpeng, X.; Cheng, R.; Sivadas, N.; Huang, B.; Schmidgall, E.; Taniguchi, T.; Watanabe, K.; McGuire, M. A.; Yao, W.; Xiao, D.; Fu, K.-M. C.; Xu, X. Van der Waals engineering of ferromagnetic semiconductor heterostructures for spin and valleytronics. *Sci. Adv.* **2017**, *3*, No. e1603113.

(24) Wu, S.; Ross, J. S.; Liu, G.-B.; Aivazian, G.; Jones, A.; Fei, Z.; Zhu, W.; Xiao, D.; Yao, W.; Cobden, D.; Xu, X. Electrical tuning of valley magnetic moment through symmetry control in bilayer MoS_2. *Nat. Phys.* **2013**, *9*, 149−153.

(25) Shinokita, K.; Wang, X.; Miyauchi, Y.; Watanabe, K.; Taniguchi, T.; Matsuda, K. Continuous Control and Enhancement of Excitonic Valley Polarization in Monolayer WSe_2 by Electrostatic Doping. *Adv. Funct. Mater.* **2019**, *29*, No. 1900260.

(26) Feng, S.; Cong, C.; Konabe, S.; Zhang, J.; Shang, J.; Chen, Y.; Zou, C.; Cao, B.; Wu, L.; Peimyoo, N.; Zhang, B.; Yu, T. Engineering Valley Polarization of Monolayer WS_2: A Physical Doping Approach. *Small* **2019**, *15*, No. 1805503.

(27) Jones, A. M.; Yu, H.; Ghimire, N. J.; Wu, S.; Aivazian, G.; Ross, J. S.; Zhao, B.; Yan, J.; Mandrus, D. G.; Xiao, D.; Yao, W.; Xu, X. Optical generation of excitonic valley coherence in monolayer WSe_2. *Nat. Nanotechnol.* **2013**, *8*, 634−638.

(28) Konabe, S. Screening effects due to carrier doping on valley relaxation in transition metal dichalcogenide monolayers. *Appl. Phys. Lett.* **2016**, *109*, No. 073104.

(29) Miyauchi, Y.; Konabe, S.; Wang, F.; Zhang, W.; Hwang, A.; Hasegawa, Y.; Zhou, L.; Mouri, S.; Toh, M.; Eda, G.; Matsuda, K. Evidence for line width and carrier screening effects on excitonic valley relaxation in 2D semiconductors. *Nat. Commun.* **2018**, *9*, No. 2598.

(30) Kim, C.; Moon, I.; Lee, D.; Choi, M. S.; Ahmed, F.; Nam, S.; Cho, Y.; Shin, H.-J.; Park, S.; Yoo, W. J. Fermi Level Pinning at Electrical Metal Contacts of Monolayer Molybdenum Dichalcogenides. *ACS Nano* **2017**, *11*, 1588−1596.

(31) Hanbicki, A.; Currie, M.; Kioseoglou, G.; Friedman, A.; Jonker, B. Measurement of high exciton binding energy in the monolayer transition-metal dichalcogenides WS_2 and WSe_2. *Solid State Commun.* **2015**, *203*, 16−20.

(32) Chernikov, A.; Berkelbach, T. C.; Hill, H. M.; Rigosi, A.; Li, Y.; Aslan, B.; Reichman, D. R.; Hybertsen, M. S.; Heinz, T. F. Exciton Binding Energy and Nonhydrogenic Rydberg Series in Monolayer WS_2. *Phys. Rev. Lett.* **2014**, *113*, No. 076802.

(33) Klots, A. R.; Newaz, A. K. M.; Wang, B.; Prasai, D.; Krzyzanowska, H.; Lin, J.; Caudel, D.; Ghimire, N. J.; Yan, J.; Ivanov, B. L.; Velizhanin, K. A.; Burger, A.; Mandrus, D. G.; Tolk, N. H.; Pantelides, S. T.; Bolotin, K. I. Probing excitonic states in suspended two-dimensional semiconductors by photocurrent spectroscopy. *Sci. Rep.* **2014**, *4*, No. 6608.

https://doi.org/10.1021/acsanm.4c07356
ACS Appl. Nano Mater. 2025, 8, 7520−7529

(34) Berkelbach, T. C.; Hybertsen, M. S.; Reichman, D. R. Theory of neutral and charged excitons in monolayer transition metal dichalcogenides. *Phys. Rev. B* **2013**, *88*, No. 045318.
(35) Mitioglu, A. A.; Plochocka, P.; del Aguila, Á. G.; Christianen, P. C. M.; Deligeorgis, G.; Anghel, S.; Kulyuk, L.; Maude, D. K. Optical Investigation of Monolayer and Bulk Tungsten Diselenide (WSe_2) in High Magnetic Fields. *Nano Lett.* **2015**, *15*, 4387−4392.
(36) Wang, G.; Bouet, L.; Lagarde, D.; Vidal, M.; Balocchi, A.; Amand, T.; Marie, X.; Urbaszek, B. Valley dynamics probed through charged and neutral exciton emission in monolayer WSe_2. *Phys. Rev. B* **2014**, *90*, No. 075413.
(37) Mak, K. F.; He, K.; Shan, J.; Heinz, T. F. Control of valley polarization in monolayer MoS_2 by optical helicity. *Nat. Nanotechnol.* **2012**, *7*, 494−498.
(38) Zeng, H.; Dai, J.; Yao, W.; Xiao, D.; Cui, X. Valley polarization in MoS_2 monolayers by optical pumping. *Nat. Nanotechnol.* **2012**, *7*, 490−493.
(39) Lin, Z.; Liu, Y.; Wang, Z.; Xu, S.; Chen, S.; Duan, W.; Monserrat, B. Phonon-Limited Valley Polarization in Transition-Metal Dichalcogenides. *Phys. Rev. Lett.* **2022**, *129*, No. 027401.
(40) Novikov, A. Experimental measurement of work function in doped silicon surfaces. *Solid-State Electron.* **2010**, *54*, 8−13.
(41) Nikolaou, N.; Dimitrakis, P.; Normand, P.; Skarlatos, D.; Giannakopoulos, K.; Mergia, K.; Ioannou-Sougleridis, V.; Kukli, K.; Niinistö, J.; Mizohata, K.; Ritala, M.; Leskelä, M. Inert ambient annealing effect on MANOS capacitor memory characteristics. *Nanotechnology* **2015**, *26*, No. 134004.
(42) Liu, W.; Cao, W.; Kang, J.; Banerjee, K. (Invited) High-Performance Field-Effect-Transistors on Monolayer-WSe_2. *ECS Trans.* **2013**, *58*, 281.
(43) Xia, P.; Feng, X.; Ng, R. J.; Wang, S.; Chi, D.; Li, C.; He, Z.; Liu, X.; Ang, K.-W. Impact and Origin of Interface States in MOS Capacitor with Monolayer MoS_2 and HfO_2 High-k Dielectric. *Sci. Rep.* **2017**, *7*, No. 40669.
(44) Di Bartolomeo, A.; Genovese, L.; Giubileo, F.; Iemmo, L.; Luongo, G.; Foller, T.; Schleberger, M. Hysteresis in the transfer characteristics of MoS_2 transistors. *2D Mater.* **2018**, *5*, No. 015014.
(45) Rong, K.; Noro, R.; Nishigaki, H.; Ding, M.; Yao, Y.; Inoue, T.; Katayama, R.; Kobayashi, Y.; Matsuda, K.; Mouri, S. Far-Reaching Remote Doping for Monolayer MoS_2 Using a Ferroelectric Substrate: Unveiling the Impact of h-BN Spacer Thickness. *ACS Appl. Electron. Mater.* **2024**, *6*, 5914−5922.
(46) Shen, P.-C.; Lin, C.; Wang, H.; Teo, K. H.; Kong, J. Ferroelectric memory field-effect transistors using CVD monolayer MoS_2 as resistive switching channel. *Appl. Phys. Lett.* **2020**, *116*, No. 033501.
(47) Guo, Y.; Wei, X.; Shu, J.; Liu, B.; Yin, J.; Guan, C.; Han, Y.; Gao, S.; Chen, Q. Charge trapping at the MoS_2-SiO_2 interface and its effects on the characteristics of MoS_2 metal-oxide-semiconductor field effect transistors. *Appl. Phys. Lett.* **2015**, *106*, No. 103109.
(48) Maialle, M. Z.; de Andrada e Silva, E. A.; Sham, L. J. Exciton spin dynamics in quantum wells. *Phys. Rev. B* **1993**, *47*, No. 15776.
(49) Mai, C.; Barrette, A.; Yu, Y.; Semenov, Y. G.; Kim, K. W.; Cao, L.; Gundogdu, K. Many-Body Effects in Valleytronics: Direct Measurement of Valley Lifetimes in Single-Layer MoS_2. *Nano Lett.* **2014**, *14*, 202−206.
(50) Khakbaz, P.; Driussi, F.; Giannozzi, P.; Gambi, A.; Lizzit, D.; Esseni, D. Engineering of metal-MoS_2 contacts to overcome Fermi level pinning. *Solid-State Electron.* **2022**, *194*, No. 108378.
(51) Dagan, R.; Vaknin, Y.; Rosenwaks, Y. Gap state distribution and Fermi level pinning in monolayer to multilayer MoS_2 field effect transistors. *Nanoscale* **2020**, *12*, 8883−8889.
(52) Kim, G.-S.; Kim, S.-H.; Park, J.; Han, K. H.; Kim, J.; Yu, H.-Y. Schottky Barrier Height Engineering for Electrical Contacts of Multilayered MoS_2 Transistors with Reduction of Metal-Induced Gap States. *ACS Nano* **2018**, *12*, 6292−6300.
(53) Ross, J. S.; Wu, S.; Yu, H.; Ghimire, N. J.; Jones, A. M.; Aivazian, G.; Yan, J.; Mandrus, D. G.; Xiao, D.; Yao, W.; Xu, X. Electrical control of neutral and charged excitons in a monolayer semiconductor. *Nat. Commun.* **2013**, *4*, No. 1474.
(54) Mouri, S.; Miyauchi, Y.; Matsuda, K. Tunable Photoluminescence of Monolayer MoS_2 via Chemical Doping. *Nano Lett.* **2013**, *13*, 5944−5948.
(55) Pan, Y.; Rahaman, M.; He, L.; Milekhin, I.; Manoharan, G.; Aslam, M. A.; Blaudeck, T.; Willert, A.; Matković, A.; Madeira, T. I.; Zahn, D. R. T. Exciton tuning in monolayer WSe_2 via substrate induced electron doping. *Nanoscale Adv.* **2022**, *4*, 5102−5108.
(56) Lin, Y.; Ling, X.; Yu, L.; Huang, S.; Hsu, A. L.; Lee, Y.-H.; Kong, J.; Dresselhaus, M. S.; Palacios, T. Dielectric Screening of Excitons and Trions in Single-Layer MoS_2. *Nano Lett.* **2014**, *14*, 5569−5576.
(57) Mouri, S.; Zhang, W.; Kozawa, D.; Miyauchi, Y.; Eda, G.; Matsuda, K. Thermal dissociation of inter-layer excitons in MoS_2/$MoSe_2$ hetero-bilayers. *Nanoscale* **2017**, *9*, 6674−6679.
(58) Kwon, J.; Lee, J.-Y.; Yu, Y.-J.; Lee, C.-H.; Cui, X.; Hone, J.; Lee, G.-H. Thickness-dependent Schottky barrier height of MoS_2 field-effect transistors. *Nanoscale* **2017**, *9*, 6151−6157.
(59) Wang, Z.; Li, Q.; Chen, Y.; Cui, B.; Li, Y.; Besenbacher, F.; Dong, M. The ambipolar transport behavior of WSe_2 transistors and its analogue circuits. *NPG Asia Mater.* **2018**, *10*, 703−712.
(60) Kim, H.-C.; Kim, H.; Lee, J.-U.; Lee, H.-B.; Choi, D.-H.; Lee, J.-H.; Lee, W. H.; Jhang, S. H.; Park, B. H.; Cheong, H.; Lee, S.-W.; Chung, H.-J. Engineering Optical and Electronic Properties of WS_2 by Varying the Number of Layers. *ACS Nano* **2015**, *9*, 6854−6860.
(61) Schulman, D. S.; Arnold, A. J.; Das, S. Contact engineering for 2D materials and devices. *Chem. Soc. Rev.* **2018**, *47*, 3037−3058.
(62) Wang, Y.; Kim, J. C.; Li, Y.; Ma, K. Y.; Hong, S.; Kim, M.; Shin, H. S.; Jeong, H. Y.; Chhowalla, M. P-type electrical contacts for 2D transition-metal dichalcogenides. *Nature* **2022**, *610*, 61−66.
(63) Chen, S.-Y.; Goldstein, T.; Taniguchi, T.; Watanabe, K.; Yan, J. Coulomb-bound four- and five-particle intervalley states in an atomically-thin semiconductor. *Nat. Commun.* **2018**, *9*, No. 3717.
(64) Lin, K.-Q.; Ziegler, J. D.; Semina, M. A.; Mamedov, J. V.; Watanabe, K.; Taniguchi, T.; Bange, S.; Chernikov, A.; Glazov, M. M.; Lupton, J. M. High-lying valley-polarized trions in 2D semiconductors. *Nat. Commun.* **2022**, *13*, No. 6980.
(65) Zhang, Q.; Sun, H.; Tang, J.; Dai, X.; Wang, Z.; Ning, C.-Z. Prolonging valley polarization lifetime through gate-controlled exciton-to-trion conversion in monolayer molybdenum ditelluride. *Nat. Commun.* **2022**, *13*, No. 4101.
(66) Laturia, A.; Van de Put, M. L.; Vandenberghe, W. G. Dielectric properties of hexagonal boron nitride and transition metal dichalcogenides: from monolayer to bulk. *npj 2D Mater. Appl.* **2018**, *2*, No. 6.
(67) Lee, C.; Rathi, S.; Khan, M. A.; Lim, D.; Kim, Y.; Yun, S. J.; Youn, D.-H.; Watanabe, K.; Taniguchi, T.; Kim, G.-H. Comparison of trapped charges and hysteresis behavior in hBN encapsulated single MoS_2 flake based field effect transistors on SiO_2 and hBN substrates. *Nanotechnology* **2018**, *29*, No. 335202.
(68) Das, S.; Huang, D.; Verzhbitskiy, I. A.; Ooi, Z.-E.; Lau, C. S.; Lee, R.; Wong, C. P. Y.; Goh, K. E. J. Electrical Control of Valley Polarized Charged Exciton Species in Monolayer WS_2. *ACS Nano* **2024**, *18*, 30805−30815.

https://doi.org/10.1021/acsanm.4c07356
ACS Appl. Nano Mater. 2025, 8, 7520−7529